

Effect of annealing on physicochemical and photocatalytic activity of Cu_{5%} loading on ZnO synthesized by sol–gel method

A. Modwi^{1,4} · M. A. Abbo^{2,4} · E. A. Hassan⁴ · Ammar Houas^{1,3}

Received: 10 May 2016 / Accepted: 25 July 2016 / Published online: 4 August 2016
© Springer Science+Business Media New York 2016

Abstract In this study, mesoporous Zn_{0.95}Cu_{0.05}O was prepared using a simple sol-gel method in the presence of tartaric acid as catalyst. The obtained powders were annealed under air in the range of T_C: 250–550 °C for Zn_{0.95}Cu_{0.05}O. The ratio of Cu:Zn obtained from energy dispersive X-ray (EDX) (4.8 %) is in good agreement with the desired experimental result. The X-ray diffraction analysis indicated that the wurtzite structure was maintained for all samples and copper was successfully doped into ZnO at low T_C. However, the formation of monoclinic CuO was observed at higher T_C. For Zn_{0.95}Cu_{0.05}O, the crystallite size increased with the annealing temperature from 15.86 to 24.24 nm. The isotherms obtained were type IV with a hysteresis type H₃, confirming the mesoporous behavior of the catalysts. The surface area was in the range of 35.1 to 8.66 m²/g. All the prepared catalysts mainly showed two emission regions: a sharp peak in the ultraviolet region and another broad peak in the visible region. The photocatalytic activity was achieved by the degradation of 300 mg/L malachite green (MG) aqueous solution under UV irradiation. The findings showed that the

increased annealing of Cu_{5%} doped ZnO with CuO on the surface resulted in highly improved photocatalytic activity.

1 Introduction

Over the past decade, the synthesis and use of semiconductors in various areas of technology has attracted much attention and interest. Particularly in the field of water and gas treatment because of the ability of some metal oxides, such as ZnO and TiO₂, to serve as photocatalysts [1–3]. ZnO is one of the most recently utilized semiconductors, due to its direct band gap of 3.37 eV and large exciton binding energy of 60 meV at room temperature [4–7]. The important advantages of ZnO include its ability to absorb a large quantity of visible light than TiO₂, environmental sustainability, its low cost and high catalytic efficiency [8–11]. For this reason, ZnO is suitable and more effective in the photocatalytic degradation of some dyes [12–14]. Hence, there are great research efforts to enhance the ZnO photocatalyst.

Many synthesis parameters can strongly affect the photocatalytic performances of prepared nanoparticles such as the nature of solvent and or surfactant [15, 16]. Annealing and doping are important approaches used to improve ZnO as a photocatalyst and are more effective and play important roles in controlling the intrinsic defects of ZnO. Moreover, annealing increases the crystallinity of ZnO, decreases the defect on its surface, and reduces its band gap energy [17, 18]. Transitions metal doping ZnO helps in improving charge separation between electrons and holes through the formation of electron traps. However, numerous transition metals are widely used in doped ZnO, such as V, Co, Al, Fe, Cu, etc. [19–23]. Among these, Cu may be an important and more effective doping element

✉ A. Modwi
abuelizkh81@gmail.com

¹ Department of Chemistry, College of Sciences, Al Imam Mohammad Ibn Saud Islamic University (IMSIU), Riyadh 11623, Saudi Arabia

² Chemistry Department, College of Education and Science, Taif University, Taif, Saudi Arabia

³ Unité de Recherche Catalyse et Matériaux pour l'Environnement et les Procédés (URCMEP), Université de Gabès, Campus Universitaire-Cité Erriadh, 6072 Gabès, Tunisia

⁴ Chemistry Department, College of Science, Sudan University of Science and Technology, Khartoum, Sudan

for improving ZnO as a photocatalyst [24]. Copper loading into ZnO creates defects in the lattice, which enhances photocatalytic activity. Kuriakose et al. [25] reported the synthesis of Cu doped ZnO nanostructures and showed that 5 % Cu doped ZnO was the most efficient photocatalyst, and this could be attributed to the formation of excess CuO on the surface. Therefore, more studies should be conducted to enhance the use of 5 % Cu-doped ZnO as a photocatalyst.

Cu-doped ZnO can be synthesized by various methods such as Sol-gel [26], spray pyrolysis [27], electrochemical deposition [28], vapour-phase transport [29], hydrothermal [30], ultrasonic method [31] and co-precipitation [32–34]. The most important and common method of preparing nanoparticles is the sol-gel method, due the high purity and crystallinity of the obtained materials [35, 36].

In this study, a simple sol-gel synthesis of mesoporous $\text{Zn}_{0.95}\text{Cu}_{0.05}\text{O}$ using tartaric acid was reported. The obtained nanostructure products were characterized by scanning electron microscopy (SEM), energy dispersive X-ray (EDX), X-ray diffraction analysis (XRD), Brunauer-Emmett-Teller method (BET), Fourier transform infrared (FTIR), thermogravimetric analysis (TGA) and photoluminescence (PL). Also, the effect of annealing temperature on their physicochemical properties and the MG photocatalytic degradation under UV irradiation were discussed. This study demonstrated that Cu₅ % doped ZnO, at higher annealing temperature with CuO present on the surface, produced highly photocatalytic activity.

2 Experimental

2.1 Synthesis of pure ZnO and Cu doped ZnO nanoparticles

Zinc acetate dihydrate [$\text{Zn}(\text{CH}_3\text{COO})_2 \cdot 2\text{H}_2\text{O}$], absolute methanol 99.99 %, tartaric acid ($\text{CHOH}-\text{COOH}$)₂, cupric nitrate trihydrate [$\text{Cu}(\text{NO}_3)_2 \cdot 3\text{H}_2\text{O}$] and malachite green (MG) were purchased from Panreac (in Spain). All chemicals were utilized without further purification. A certain amount of zinc acetate dehydrate (as precursor) was dissolved in 75 mL of methanol, after stirring for 30 min, an appropriate amount of copper nitrate trihydrate with a molar ratio Cu/Zn of 5.26 % was also added and the mixture was stirred for 30 min. On the other hand, an amount of double distilled water solution (45 mL) of tartaric acid was added dropwise to the previous mixture. The gel formed rapidly (5 min) at room temperature under vigorous magnetic stirring and dried at 85 °C for 16 h. Subsequently, the dry gel was first grinded and annealed at 250, 350, 450 and 550 °C for 1 h. The pure ZnO

nanomaterial was synthesized following the same procedure without adding copper nitrate trihydrate.

2.2 Characterization techniques

The morphology of the nanopowder samples was examined using a scanning electron microscope. The samples were previously oven dried at 105 °C and coated with a thin film of gold to provide ZnO powder surface with electrical conduction. The composition and average size of nanoparticles were determined by the powder X-ray diffraction patterns, the samples were recorded by a diffractometer (D8 Advance Bruker), using Cu-K α radiation ($\lambda = 0.15406$ nm). The accelerating voltage and scanning angle were 40 kV and 20°–75°, respectively. The mode of chemical bonding in the prepared samples was studied by Fourier transform infrared spectroscopy (Model: Nicolet 6700) in the range 4000–400 cm^{-1} with a resolution of 4 cm^{-1} . The surface area and pore sizes of nanoparticles were determined by the Brunauer-Emmett-Teller (BET) method using a Micrometrics ASAP 2020 apparatus (degas temperature: ambient to 200 °C for 20 min with pressure range of 0 to 950 mmHg). The thermal decomposition behaviors of samples were evaluated using thermogravimetry (Model: Mettler Toledo). A heating rate of 0.02 to 250 °C/min, room temperature of 1100 °C and crucible volume of up to 150 μL were utilized. A Perkin Elmer LS45 luminescence (PL) was used to study the spectra of fluorescence. The apparatus were operated at room temperature and the excitation source was a special Xenon flash tube that produces an intense short duration pulse of radiation over the spectral range. The excitation wavelength was 325 nm.

2.3 Determination of heterogeneous photocatalytic activity

The photoactivities of purely prepared ZnO and Cu-doped ZnO were examined using (MG) dye as a pollutant and all experiments were carried out in a Pyrex photoreactor under U.V irradiation. After achieving adsorption equilibrium in the dark, the solution was illuminated for photocatalytic kinetic study: The samples of the MG solution were taken after different irradiation times and were analyzed using UV-visible spectroscopy at a wavelength $\lambda_{\text{max}} = 618$ nm. Using the Beer-Lambert law, the absorption measurement was converted to concentration. The photocatalytic degradation efficiency was calculated using the following equation:

$$\text{MG degradation \%} = \left[\frac{(\text{C}_0 - \text{C}_t)}{\text{C}_0} \right] \times 100 \quad (1)$$

where, C_0 is the (MG) initial concentration (fixed at 300 mg/L) and, C_t is the MG concentration at time t .

3 Results and discussion

3.1 Scanning electron microscopy (SEM) image and energy dispersive analysis X-ray (EDX) spectra

Figure 1a, b show the SEM micrographs of pure ZnO and $Zn_{0.95}Cu_{0.05}O$ annealed at 550 °C. The particles of the obtained powder are spherical in shape with a little agglomeration. Table 1 shows the weight percentages of the elements. The calculated Cu/Zn weight ratio was found to be equal to 0.048 (4.8 %), which corresponds to 4.6 % Cu/Zn as a molar ratio. This result is in good agreement with the desired experimental ratio shown above (5.26 %).

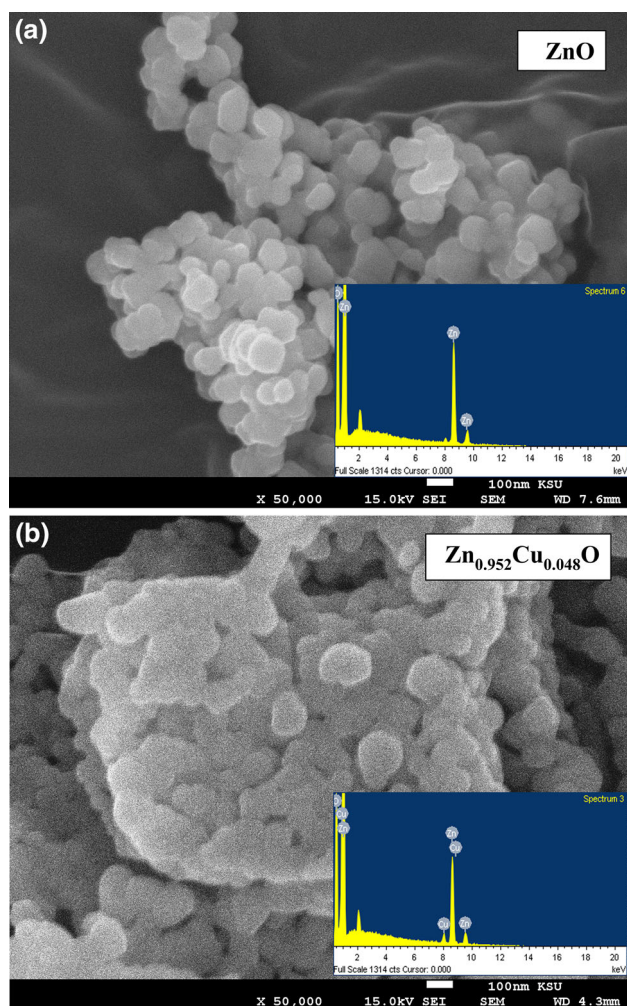


Fig. 1 SEM and EDAX results of **a** ZnO pure and **b** $Zn_{0.95}Cu_{0.05}O$

Table 1 Weight percentage of the elements obtained from (EDAX)

Samples	Weight percentage of the elements (%)		
	O	Zn	Cu
ZnO	16.53	83.47	–
$Zn_{0.95}Cu_{0.05}O$	16.00	80.22	3.89

Thus, based on the average molar ratio, the Cu-doped ZnO formula can be considered as $Zn_{0.95}Cu_{0.05}O$.

3.2 Characterization of the prepared catalysts by X-ray diffraction

The XRD patterns for ZnO and $Zn_{0.95}Cu_{0.05}O$ nanoparticles are shown in Fig. 2a. The results show broad peaks at positions 31.61°, 34.39°, 36.11°, 47.40°, 56.52°, 62.72°, 66.29°, 67.91° and 69.08° of the spectra. These values are

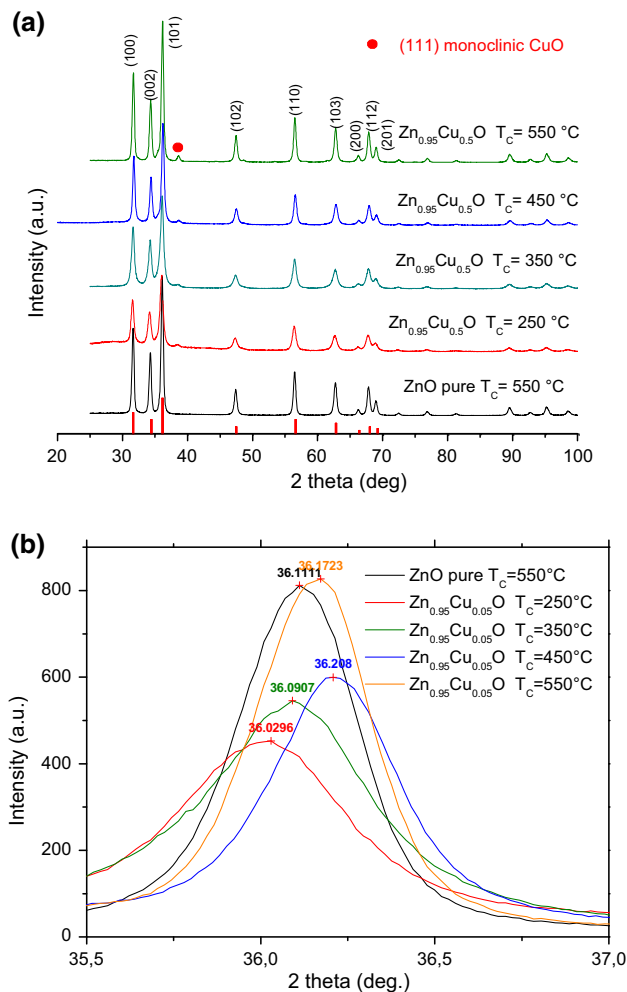


Fig. 2 **a** XRD patterns of pure ZnO at $T_C = 550$ °C and $Zn_{0.95}Cu_{0.05}O$ catalysts at $T_C = 250, 350, 450$ and 550 °C. **b** XRD principal peak shift due to the effects of the Cu doping and T_C

in good agreement with the standard card file (JCPDS 36-1451) for ZnO and can be indexed as the hexagonal wurtzite structure. In addition, the appearance of a very low-intensity diffraction peak at position 38.65°, corresponding to CuO as the monoclinic (base-centered) phase (JCPDS#18-1916) was observed. The appearance of this peak is due to the high quantity of doped Cu and can be detected by XRD. The average crystallite size (D) of the prepared nanomaterial shown in Table 2 was calculated using Scherrer’s equation:

$$D = \frac{0.9\lambda}{\beta \cos\theta} \tag{2}$$

where λ is the wavelength of Cu K α radiation, β is the full width half maxima (FWHM) of the diffraction peak and θ is the Bragg peak angle. The average particle size of ZnO (pure) was found to be 22.26 nm.

The effect of Cu doping can be observed at the same annealing temperature ($T_C = 550\text{ }^\circ\text{C}$) as shown in Fig. 2b. In comparison with pure ZnO, the introduction of copper ions shifted the diffraction peaks to higher angles by 0.06°. Indeed, this change can be attributed to the replacement of Zn ions (ionic radii = 0.60 Å) by Cu ions (ionic radii = 0.57 Å) or may be due to structural stresses and modification of the lattice parameters of ZnO. This shift value indicated a decrease in the lattice parameters since the value of c parameter decreased by about 0.01 Å from undoped ZnO (5.226 Å) to Cu-doped ZnO (5.217 Å). This decrease confirms that the substitution of Zn ions by Cu in the ZnO lattice, was facilitated by the similarity of the ionic radii. Sharma et al. [37], in their study on Mn-doped ZnO, reported similar observations.

The annealing temperature (T_C) effect was observed on both intensity of XRD peaks and lattice parameters as shown in Fig. 2b. The principal peak (101) intensity increased with increase in T_C , and the shape of this peak became narrower, indicating an increase in particle size. On the other hand, the effect of T_C on the lattice parameters showed the shift of the peak at $2\theta = 36.11^\circ$, which increased from $T_C = 250\text{--}450\text{ }^\circ\text{C}$ and then decreased to

$T_C = 550\text{ }^\circ\text{C}$ (Fig. 3). For Zn_{0.95}Cu_{0.05}O nanoparticles, the particle size seems to be dependent on the annealing temperature as shown in Table 2. It varied from 15.86 to 24.25 nm when the annealing temperature was in the range of 250–550 °C. The increase in the particle size with the annealing temperature (Fig. 3), may be due to the agglomeration of the particles. Consequently, the specific surface area of the samples was decreased in the range of the temperature from 250 to 550 °C (Table 3).

3.3 Fourier transform infrared studies (FTIR)

The chemical bonding and formation of wurtzite structure in ZnO (pure) and Zn_{0.95}Cu_{0.05}O were confirmed by FTIR measurements at room temperature. The spectra are shown in Fig. 4. The broad absorption band at 3439.39, 1077.74, 3446.53 and 1075.74 cm⁻¹ can be attributed to the normal polymeric O-H stretching vibration of H₂O, respectively in ZnO and Zn_{0.95}Cu_{0.05}O lattices [38]. Other sharp peaks observed at 1621.45 and 1615.60 cm⁻¹ can be attributed to H–O–H bending vibration, which in turn can be assigned to the small amount of H₂O in the ZnO and Zn_{0.95}Cu_{0.05}O nanocrystals [39]. The absorption band observed between 2300 and 2400 cm⁻¹ are due to the existence of CO₂ molecule in the air [40]. The vibration band at 446.31 cm⁻¹ assigned to the stretching mode of pure ZnO, shifted to a lower frequency at 438.48 cm⁻¹ for Zn_{0.95}Cu_{0.05}O. Hence, it is supposed that Cu-ion can be successfully substituted into the crystal lattice of ZnO [41].

3.4 Surface area analysis (BET)

Figure 5 shows the nitrogen adsorption-desorption isotherms and Barrett–Joyner–Halenda (BJH) pore size distribution for pure ZnO annealed at 550 °C, and Zn_{0.95}Cu_{0.05}O at a temperature range of 250–550 °C. All the isotherms obtained are Type IV and correspond to a capillary condensation, according to the classification of the International Union for Pure and Applied Chemistry (IUPAC). The hysteresis is Type H3, and is characteristic of the

Table 2 Average crystallite sizes and lattice parameters of the undoped and Cu doped ZnO nanoparticles prepared at different annealing temperatures

Samples	2θ (degree)	Crystallite size (nm)	Lattice parameter (Å)		c/a
			(a)	(c)	
ZnO pure					
$T_C = 550\text{ }^\circ\text{C}$	36.11	22.26	3.2628	5.2256	1.6016
Zn _{0.95} Cu _{0.05} O					
$T_C = 250\text{ }^\circ\text{C}$	36.03	15.86	3.2732	5.2442	1.6022
$T_C = 350\text{ }^\circ\text{C}$	36.09	16.95	3.2608	5.2608	1.6133
$T_C = 450\text{ }^\circ\text{C}$	36.21	20.95	3.2491	5.2088	1.6031
$T_C = 550\text{ }^\circ\text{C}$	36.17	24.25	3.2588	5.2178	1.6009
JCPDS 36-1451			3.249	5.206	1.602

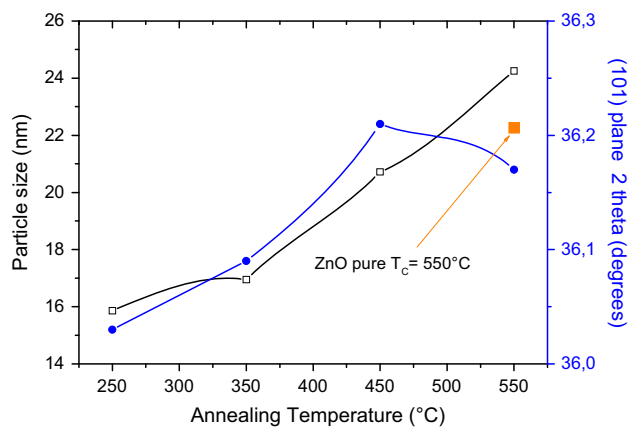


Fig. 3 Effect of annealing temperature on the crystallite size and the (101) plane two theta

mesoporous material with slit-shape pores. Based on the results obtained from Fig. 5, the adsorption of N_2 on pure and $Zn_{0.95}Cu_{0.05}O$ catalysts, slightly increased from a low relative pressure of about 0.02 to 0.8 at higher T_C (450 and 550 °C) to 0.6 at lower T_C (250 and 350 °C), and then

followed by a sharp rise from 0.6 or 0.8 and above due to substantial inter particle porosity [42]. The highest and least volume of absorbed N_2 can be attributed to the catalysts annealed at T_C equal to 250 and 550 °C, respectively. All the desorption branches are different from those of adsorption, indicating differences in their pore's texture [43]. Among all the catalysts, $Zn_{0.95}Cu_{0.05}O$ annealed at $T_C = 250$ °C showed the highest volume of adsorption and widest desorption branch as shown in Fig. 5. The Barret–Joyner–Halenda (BJH) pore size distribution for all catalysts is shown in Fig. 5. All plots are located in the mesoporous range, which is in good agreement with the Type IV adsorption isotherm. The BJH pore size distribution of pure ZnO and $Zn_{0.95}Cu_{0.05}O$ annealed at $T_C = 550$ °C (Fig. 5) indicates different features of $Zn_{0.95}Cu_{0.05}O$ annealed at $T_C = 250, 350$ and 450 °C, specifically from the average pore diameter centered at around 70 nm. This shows the result of the modification in pore texture. Based on the obtained results, it can be suggested that the annealing temperature has a clear effect on specific surface area and pore size distribution of the doped

Table 3 Structural and textural properties of prepared photocatalysts

Samples	BET surface area (m^2/g)	Pore volume (cm^3/g)	Average pore diameter (nm) Adsorption–desorption
ZnO pure			
$T_C = 550$ °C	7.48	0.053	44.03–37.38
$Zn_{0.95}Cu_{0.05}O$			
$T_C = 250$ °C	35.10	0.220	24.63–21.67
$T_C = 350$ °C	19.39	0.147	31.03–30.58
$T_C = 450$ °C	12.55	0.146	52.88–44.08
$T_C = 550$ °C	8.66	0.053	36.38–30.97

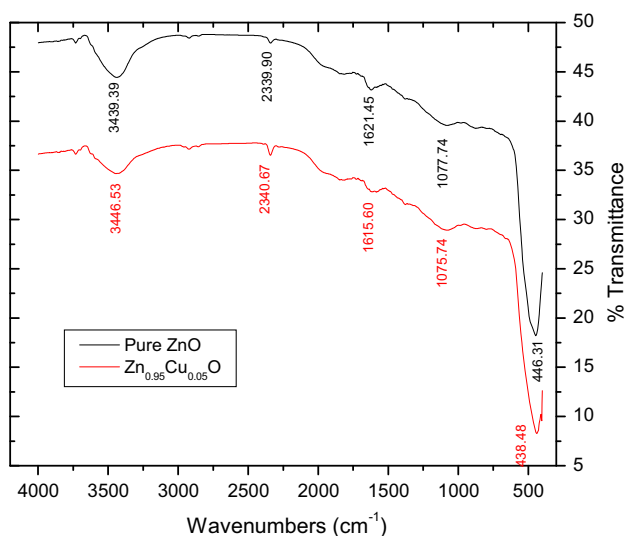


Fig. 4 FTIR spectra of pure ZnO and $Zn_{0.95}Cu_{0.05}O$ annealed at 550 °C

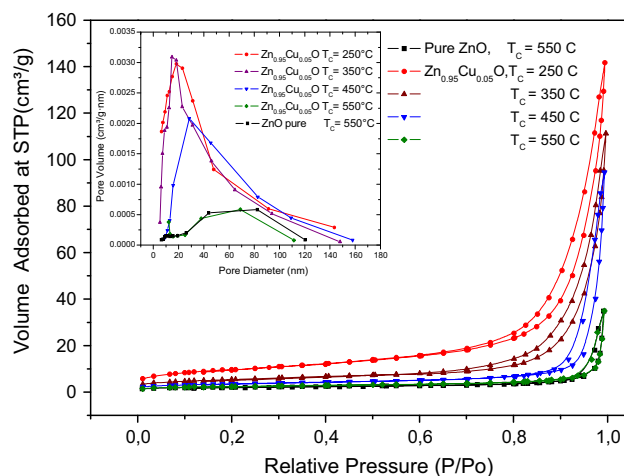


Fig. 5 N_2 adsorption-desorption isotherms and pore size distribution (inset) of Pure ZnO annealed at 550 °C and $Zn_{0.95}Cu_{0.05}O$ annealed at different temperatures

catalysts (Table 3, S_{BET} decreased from 35.1 to 8.66 m^2/g as T_C increased from 250 to 550 $^{\circ}C$). On the other hand, for the same $T_C = 550^{\circ}C$, the obtained isotherms for pure and doped ZnO are very similar, showing almost the same specific surface area. This shows that the effect of doping is less important than the annealing temperature. By increasing the annealing temperature, a remarkable decrease in surface area of pure ZnO and $Zn_{0.95}Cu_{0.05}O$ can be observed. This phenomenon could be explained by clogging pores caused by the occurrence of possible aggregation when the annealing temperature increases. This may have the effect of clogging as observed in the diminution of both volume and average pore size.

3.5 Thermal analysis of the prepared xerogel catalysts

The thermal stability of the prepared pure ZnO and $Zn_{0.95}Cu_{0.05}O$ by the fast sol–gel method was studied by TGA and DTG as shown in Fig. 6a, b. For the pure ZnO, the weight loss of the xerogel occurred principally in two steps. In the first step, weight loss (8 %) was in the range of

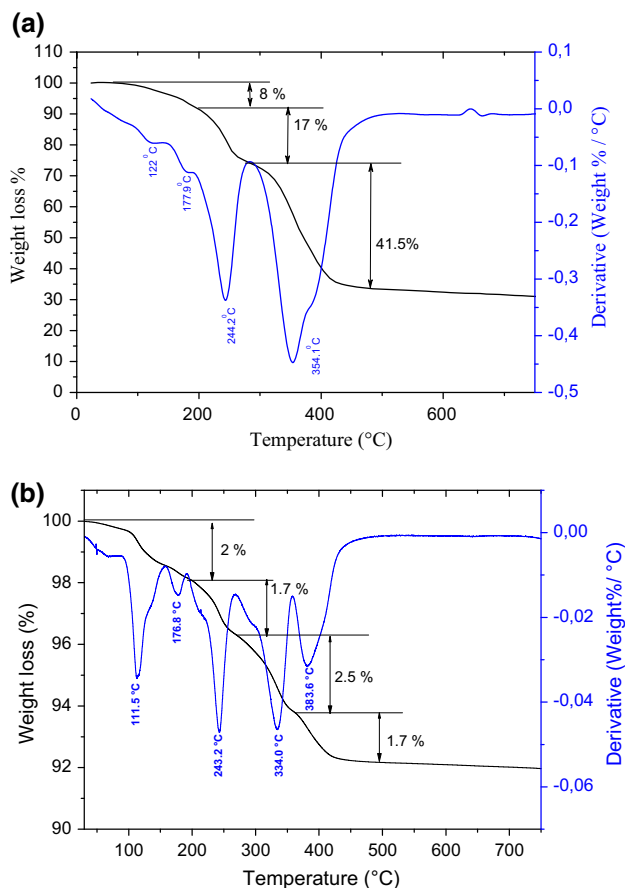


Fig. 6 TG-DTG analysis of **a** ZnO and **b** $Zn_{0.95}Cu_{0.05}O$ xerogel powders

80–178 $^{\circ}C$, due to the dehydration of the absorbed surface water, as well as hydrate from the remaining zinc acetate and methanol solvent. In the second step, weight loss occurred in the range from 190 to 244 $^{\circ}C$, which corresponds to 17 % due to the decomposition of tartaric acid. In the last step, weight loss ranged from 284 to 482 $^{\circ}C$ due to the conversion of zinc tartarate to zinc oxide and the percentage of weight loss was found to be 41.5 %. After 482 $^{\circ}C$, no weight loss was observed and zinc oxide formed was further confirmed by XRD. On the other hand, for $Zn_{0.95}Cu_{0.05}O$, a total weight loss of 7.9 % was observed in all four steps, and this is very low as compared with pure ZnO xerogel (64.5 %), indicating an increase in its stability due to the presence of Cu.

3.6 Photoluminescence

In this study the photoluminescence (PL) spectra of ZnO nanoparticles were determined to explore the effect of Cu-doping and annealing temperature on its optical properties. Figure 7 shows the emission spectrum of pure ZnO and $Zn_{0.95}Cu_{0.05}O$ catalysts, using an excitation wavelength of 325 nm at room temperature. The photoluminescence (PL) emission was observed for all the samples ($T_C = 250$ – $550^{\circ}C$) covering the range: from a short wavelength of 350 nm to a long wavelength of 550 nm. As shown in Fig. 7, all the samples show mainly two emission peaks: a sharp one in the ultraviolet (UV) region and another broad one in the visible region. The first one, which originates from the recombination of free exciton [44, 45], is clearly observed for pure ZnO at 379 nm. Thus, $Zn_{0.95}Cu_{0.05}O$ was annealed at the highest temperature $T_C = 550^{\circ}C$ at 385 nm, and this may be attributed to

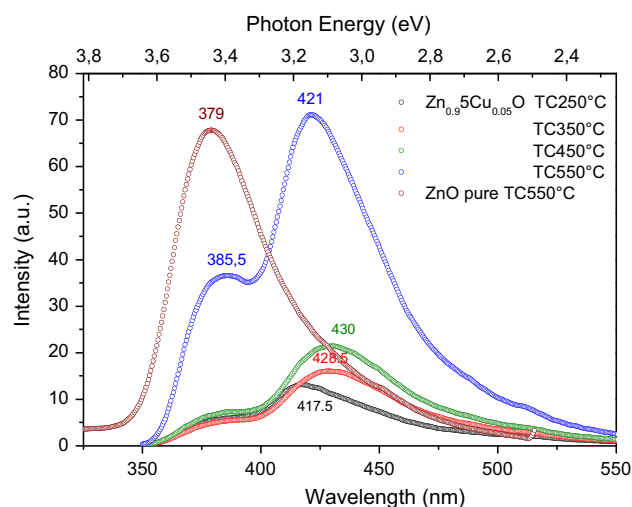


Fig. 7 PL spectra of the pure ZnO annealed at 550 $^{\circ}C$ and $Zn_{0.95}Cu_{0.05}O$ annealed at different temperatures (from $T_C = 250$ – $550^{\circ}C$), at wavelength 325 nm excitation

exciton-related near-band edge emission (NBE). The second peak was observed according to the annealing temperature T_C at 417, 421, 428.5 and 430 nm, which corresponds to the blue emission [46]. As can be seen, the second peak seems to be observed only for $Zn_{0.95}Cu_{0.05}O$ catalysts, while the intensity of both peaks depends strongly on the annealing temperature. As the annealing temperature increases, the ultraviolet emission peak of the pure ZnO and $Zn_{0.95}Cu_{0.05}O$ catalysts gradually increases especially for $T_C = 550$ °C. This increase was also observed for the blue emission peak for all annealing temperatures.

For further understanding of the PL analysis, Fig. 8 shows that all PL spectra are well fitted with a Gaussian function (the lowest correlation coefficient is 99.4 %). For pure ZnO, the deconvoluted PL spectrum (Fig. 8a) shows three peaks (Table 4): two UV emission peaks of approximately the same intensity at 373 and 389 nm corresponding to the near-band emission of ZnO [47] and a violet emission peak at 410 nm with lower intensity. The effect of Cu doping can be seen at the same $T_C = 550$ °C. By comparison of Fig. 8a, b, it was observed that there is a red-shift of approximately 5 nm in the Cu-doped sample, which may correspond to a reduction of the ZnO band gap due to Cu doping and the substitution of Cu ions into the Zn sites in the lattice as reported in the XRD study. Xu et al. [48] and Udayabhaskar et al. [49] reported similar results on Cu-doped ZnO, Ni-doped ZnO and Ca-doped ZnO materials, respectively. They observed that the violet peak at 410 in the pure ZnO completely disappeared, and this may be attributed to the defects and/or lattice imperfections of the ZnO sample, which can be removed by low-temperature thermal annealing. However, it seems that the peak was replaced by the two blue emission peaks in the $Zn_{0.95}Cu_{0.05}O$ mesoporous catalysts. The observation of visible emissions may be related to intrinsic defects in ZnO, and their enhancement in the presence of Cu ions induced a poorer crystallinity and greater level of structural defects, which can be attributed to the more intrinsic defects introduced by Cu ion incorporation into the ZnO lattice. This result is in line with the above XRD findings. Xu et al. [48] related similar results to Raman's observations regarding the defects generated gradually with the Cu doping ratio.

The effect of annealing temperature T_C and its comparison is shown in Table 4 and Fig. 8a–e, respectively. As the annealing temperature increased from 250 to 550 °C, all UV and visible luminescence increased. The increase in UV emission may be ascribed to the improvement in observed crystalline quality due to annealing. The enhancement in blue emissions intensities is likely due to the strong exchange interactions between Zn and the secondary phase formed by Cu, after annealing of the sample.

Certainly, thermal annealing can provide more energy for the substitution of Zn atom sites by Cu atoms into the lattice of ZnO.

3.7 Characterization of pure ZnO and $Zn_{0.95}Cu_{0.05}O$ by photocatalytic degradation of Malachite Green

The photocatalytic performances of pure ZnO and $Zn_{0.95}Cu_{0.05}O$ samples were investigated under UV light through the degradation of Malachite Green (MG), as a model organic pollutant. Figure 9 shows the photodegradation activity of ZnO annealed at 550 °C and $Zn_{0.95}Cu_{0.05}O$ annealed at T_C of 250–550 °C photocatalysts. The results show that no that there is no degradation in the absence of the photocatalyst. On the other hand, the photocatalytic activity of pure ZnO was found to be very low: only 15 % of MG was degraded after 2 h of irradiation. However, after doping ZnO with copper significantly increased its photocatalytic efficiency towards the degradation of MG. However, the efficiency of ZnO was significantly increased after doping with copper. As observed in Fig. 9, the kinetics were well fitted to pseudo first order then, the obtained values of the rate constant using Origin.8 software were plotted against the annealing temperature.

It's known that the photocatalytic activity is related to the surface area of the photocatalyst. The present results were showed that the Cu-doping ZnO and the annealing temperature have played a crucial role on the enhancement of the photocatalytic efficiency by increasing the surface area. Nevertheless, this is not simply a question of specific surface area and adsorption, despite the fact that adsorption is a very important step in the photocatalytic process. Figure 10 shows the adsorption in the dark, which depends to the nature of the catalyst. The most adsorbed quantity of the MG was found over the Cu-doped catalyst annealed at $T_C = 250$ °C. This result is in a good agreement with the obtained specific surface area value (35.10 m²/g), but this catalyst was found to be less photoactive towards MG degradation, among other Cu-doped catalysts.

It is also important to note that the photocatalytic efficiency towards the degradation of MG with $Zn_{0.95}Cu_{0.05}O$ increased with increase in annealing temperature and formation of a CuO phase on the surface. This clearly demonstrates that photocatalytic activity depends on the annealing temperature rather than particles size and surface area. Similarly, it was shown that the photocatalytic activity of a catalyst is related to its microstructure, such as crystal plane, crystallinity, surface properties, BET specific surface area, etc.. [50, 51]. Many studies have shown that the difference in photocatalytic activity among all catalysts, not only related to the surface adsorption ability, but also to the type and concentration of oxygen defects on the

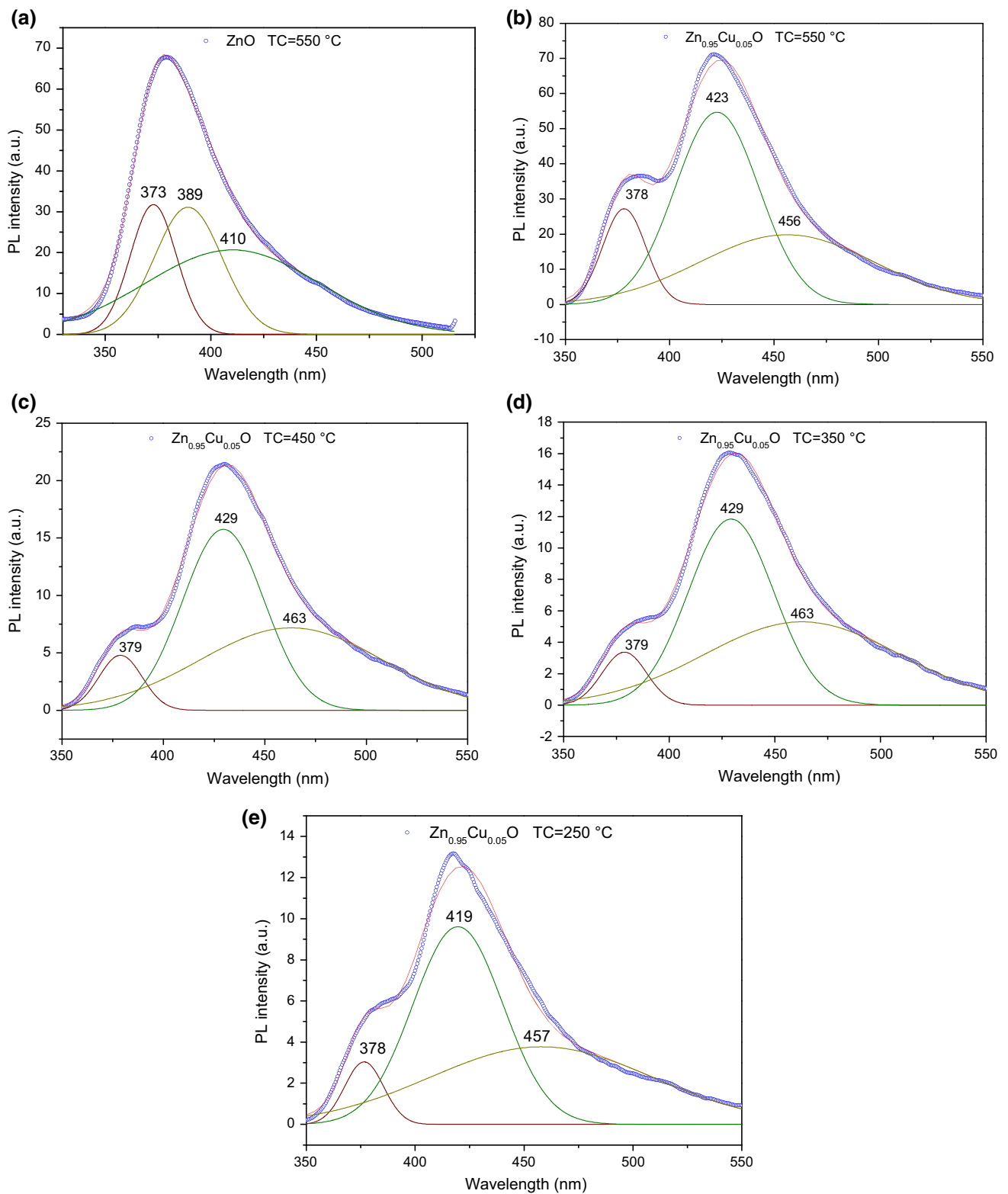
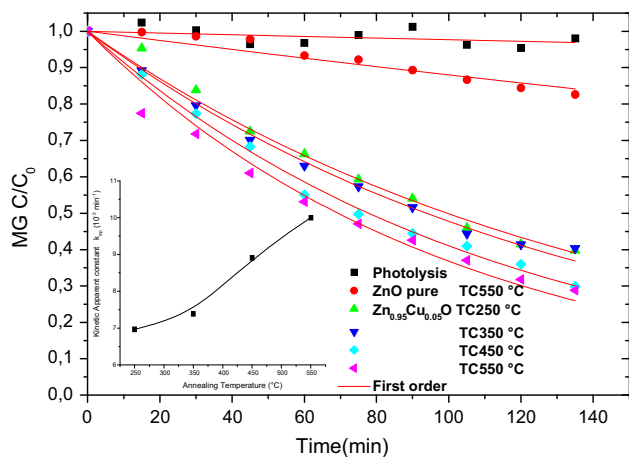
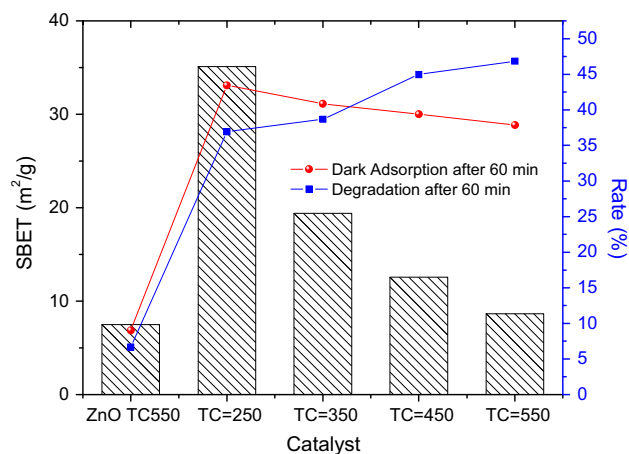


Fig. 8 PL emissions spectra of **a** pure ZnO TC = 550 °C, **b** Zn_{0.95}Cu_{0.05}O TC = 250 °C, **c** TC = 350 °C, **d** TC = 450 °C and **e** TC = 550 °C NPs using the excitation wavelength at 325 nm

Table 4 Photoluminescence emission values of pure and Cu-doped ZnO deduced from deconvolution by Gaussian function of PL spectra

Catalysts	Near band edge NEB (nm)	NEB intensity (a.u)	Blue emission (nm)
ZnO pure			
TC = 550 °C	373,389	30, 10	410 (violet)
Zn _{0.95} Cu _{0.05} O			
TC = 550 °C	378	27, 87	423.45
TC = 450 °C	379	4, 89	429.46
TC = 350 °C	379	3, 44	429.46
TC = 250 °C	378	3, 13	419.45

**Fig. 9** Photodegradation of MG under UV irradiation in the presence and absence of mesoporous catalysts. The inset shows the related kinetics apparent constant (k_{app}) with the annealing T_C **Fig. 10** Effect of mesoporous catalysts on dark adsorption after 60 min, and degradation of (MG) after 60 min and (SBET m²/g)

surface and/or surface layers. Beside, two major parameters can be affected by the annealing temperature: the increase in crystallinity and decrease of surface OH groups. Normally, since photocatalysis is a surface phenomenon, the decrease in surface OH groups may cause a loss in photocatalytic activity. However, the highest photoactivity in terms of MG degradation rate or kinetic constant was

obtained from the catalyst annealed at the highest temperature ($T_C = 550$ °C) and with the lowest specific surface area (8.66 m²/g). Therefore, an optimal quantity of hydroxyl groups on the catalyst surface in combination with a certain degree of crystallinity, and specific kinds of oxygen defects on the surface and/or surface layers are required to achieve optimal photoactivity [52]. In this study, the increase in photocatalytic activity of Zn_{0.95}Cu_{0.05}O $T_C = 550$ °C may be attributed to the good crystallinity and oxygen defects as reported for pure ZnO [53, 54]. However, the increasing crystallinity level with annealing temperature and the introduction of the native defects in the catalyst crystal in the form of neutral (V_O), singly charged (V_O^+) or doubly charged (V_O^{++}) oxygen vacancies at higher annealing temperatures, may play a major role in the enhancement of its photocatalytic efficiency [55]. It is well known that these defects in the nanoparticles reduce the electron-hole recombination; hence increase the quantum yield and thus, enhance the photocatalytic activity. Furthermore, a high concentration of oxygen vacancies on the catalyst surface at higher annealing temperature and CuO phase can also serve as trap for electrons from the conduction band [56–58].

3.7.1 Photocatalytic degradation of MG mechanism

When mixtures of MG aqueous solution and a suspension of photocatalyst were irradiated with VU light, the green solution of MG markedly changed, as a result of the decomposition of the free radicals formed in the solution. The photocatalytic activity mechanism of Zn_{0.95}Cu_{0.05}O can be understood as follows: The Cu₅ % doped ZnO resulted in the creation of intermediate energy levels, which cause a delay in the recombination of charge carriers, thereby enhancing the photocatalytic activity. Moreover, it can be noticed that the delay in the recombination of charge carriers increases whenever the crystallinity of Zn_{0.95}Cu_{0.05}O photocatalyst is improved by the annealing temperature rise. In the mechanism of photodegradation of MG in the presence of Zn_{0.95}Cu_{0.05}O photocatalyst. The excitation of photocatalyst by UV light results to the formation of electrons $e_{(CB)}^-$ in both Cu/ZnO and CuO

Scheme 1 Proposed MG degradation mechanism

conduction bands $e^-_{\text{CB,ZnO}}$ and $e^-_{\text{CB,CuO}}$ respectively. In the same time holes h^+_{VB} are formed in both Cu/ZnO and CuO valence bands $h^+_{\text{VB,ZnO}}$ and $h^+_{\text{VB,CuO}}$ respectively. The electrons $e^-_{\text{CB,CuO}}$ are transferred to the Cu/ZnO conduction band and then convert dissolved oxygen to super oxide radical $\cdot\text{O}_2^-$. While the holes $h^+_{\text{VB,ZnO}}$ and $h^+_{\text{VB,CuO}}$ from the CuO valence band level react with water to form the strongest oxidizing agent, hydroxide free radical $\cdot\text{OH}$. Both active species can decomposed MG completely. The mechanism is schematically depicted in Scheme 1.

4 Conclusions

In summary, pure ZnO and $\text{Zn}_{0.95}\text{Cu}_{0.05}\text{O}$ nanoparticles were synthesized by a sol–gel method in the presence of tartaric acid. The obtained powders were annealed at different temperatures. XRD studies confirmed the dominant presence of hexagonal wurtzite ZnO with the formation of monoclinic CuO phase on the surface of ZnO. In this study, it was shown that specific surface area decreases with annealing temperature due to the occurrence of the aggregation phenomenon. The photocatalytic ability showed that the catalyst activity was influenced by both Cu₅ % loading on ZnO and annealing temperature. The $\text{Zn}_{0.95}\text{Cu}_{0.05}\text{O}$ catalyst annealed at 550 °C exhibited the highest photocatalytic activity due to the interlacing of several factors such as the efficient charge separation as proven by the PL spectra, the enhancement of crystallinity and the introduction of the native defects in the catalyst

crystal in the form of neutral (V_O), singly charged (V_{O^+}) or doubly charged ($\text{V}_{\text{O}^{++}}$) oxygen vacancies. Furthermore, the CuO phase on the surface resulted to delayed recombination charge and increased the photocatalytic activity of catalysts at higher temperature.

References

1. A.Y. Musa, M.M. Ba-Abbad, A.A.H. Kadhum, A.B. Mohamad, Res. Chem. Intermed. **38**, 995 (2012)
2. C. Hariharan, Appl. Catal. A **304**, 55 (2006)
3. S. Munusamy, R. Aparna, R. Prasad, Sustain. Chem. Process. **4**, 2 (2013)
4. M. Vafaei, M.S. Ghamsari, Mater. Lett. **61**, 3265 (2007)
5. C.C. Vidyasagar, Y.A. Naik, T.G. Venkatesh, R. Viswanatha, Powder Technol. **214**, 337–343 (2011)
6. Y. Wang, J. Yang, Y. Li, T. Jiang, J. Chen, J. Wang, Mater. Chem. Phys. **153**, 266–273 (2015)
7. P. Srinivasan, B. Subramanian, Y. Djaoued, J. Robichaud, T. Sharma, R. Bruning, Mater. Chem. Phys. **155**, 162–170 (2015)
8. M.A. Behnajady, N. Modirshahla, R. Hamzavi, J. Hazardous Material. B **133**, 226–232 (2006)
9. R. Ahlawat, V. Chandra Srivastava, I.D. Mall, S. Sinha, Clean **36**, 863–869 (2008)
10. D. Chu, Y. Masuda, T. Ohji, K. Kato, Langmuir **26**, 2811–2815 (2010)
11. Y. Li, W. Xie, X. Hu, G. Shen, X. Zhou, Y. Xiang, P. Fang, Langmuir **26**, 591–597 (2010)
12. C.A. Gouvêa, F. Wypych, S.G. Moraes, N. Durán, N. Nagata, P. Peralta-Zamora, Chemosphere **40**, 433–440 (2000)
13. S. Sakthivel, B. Neppolian, M.V. Shankar, B. Arabindoo, M. Palanichamy, V. Murugesan, Sol. Energy Mater. Sol. Cells **77**, 65–82 (2003)
14. A. Amine, T. Sehili, J. Pilichowski, P. Boule, J. Photochem. Photobiol. A **141**, 231–239 (2001)

15. S.M. Hosseinpour-Mashkani, M. Maddahfar, A. Sobhani-Nasab, *J. Electron. Mater.* **45**, 3612–3620 (2016)
16. S.M. Hosseinpour-Mashkani, M. Ramezani, A. Sobhani-Nasab, M. Esmaeili-Zare, *J. Mater. Sci. Mater. Electronics* **26**, 6086–6091 (2015)
17. R. Saleh, N.F. Djaja, *Spectrochim. Acta A* **130**, 581–590 (2014)
18. D. Chen, Z. Wang, T. Ren, H. Ding, W. Yao, R. Zong, Y.J. Zhu, *Phys. Chem. C* **118**, 15300 (2014)
19. A. Mhamdi, A. Labidi, B. Souissi, M. Kahlaoui, A. Yumak, K. Boubaker, A. Amlouk, M. Amlouk, *J. Alloy. Compd.* **639**, 648–658 (2015)
20. A. Franco, H.V.S. Pessoni, *Physica B* **476**, 12–18 (2015)
21. R. Yoo, S. Cho, M.-J. Song, W. Lee, *Sens. Actuators B Chem.* **221**, 217–223 (2015)
22. M.M. Ba-Abbad, A.A.H. Kadhum, A.B. Mohamad, M.S. Takriff, K. Sopian, *Chemosphere* **91**, 1604–1611 (2013)
23. B. Babu, T. Aswani, G.T. Rao, R.J. Stella, B. Jayaraja, R.V.S.S.N. Ravikumar, *J. Magn. Magn. Mater.* **355**, 76–80 (2014)
24. M. Fu, Y. Li, P. Lu, J. Liu, F. Dong, *Appl. Surf. Sci.* **258**, 1587–1591 (2011)
25. S. Kuriakose, B. Satpati, S. Mohapatra, *Phys. Chem. Chem. Phys.* **17**, 25172–25181 (2015)
26. H.J. Lee, B.S. Kim, C.R. Cho, S.Y. Jeong, *Phys. Status Solidi B Basic Res.* **241**, 1533–1536 (2004)
27. P.S. Shewale, V.B. Patil, S.W. Shin, J.H. Kim, M.D. Uplane, *Sens. Actuators B Chem.* **186**, 226–234 (2013)
28. H. Gong, J.Q. Hu, J.H. Wang, C.H. Ong, F.R. Zhu, *Sens. Actuators B Chem.* **115**, 247–251 (2006)
29. G.Z. Xing, J.B. Yi, J.G. Tao, T. Liu, L.M. Wong, Z. Zhang, T. Wu, *Adv. Mater.* **20**, 3521–3527 (2008)
30. H.W. Zhang, Z.R. Wei, Z.Q. Li, G.Y. Dong, *Mater. Lett.* **61**, 3605–3607 (2007)
31. A. Sobhani-Nasab, M. Maddahfar, S.M. Hosseinpour-Mashkani, *J. Mol. Liq.* **216**, 1–5 (2016)
32. P. Dhamodharan, R. Gobi, N. Shanmugam, N. Kannadasan, R. Poonguzhali, S. Ramya, *Spectrochim. Acta A* **131**, 125–131 (2014)
33. S. Singhal, J. Kaur, T. Namgyal, R. Sharma, *Physica B* **407**, 1223–1226 (2012)
34. Majid Ramezani, S.M. Hosseinpour-Mashkani, A. Sobhani-Nasab, H.G. Estarki, *J. Mater. Sci. Mater. Electronics* **26**, 7588–7594 (2015)
35. J. Lee, A.J. Easteal, U. Pal, D. Bhattacharyya, *Curr. Appl. Phys.* **9**, 792–796 (2009)
36. Mahnaz Maddahfar, Majid Ramezani, Masoud Sadeghi, Ali Sobhani-Nasab, *J. Mater. Sci. Mater. Electronics* **26**, 7745–7750 (2015)
37. R.K. Sharma, S. Patel, K.C. Pargaian, *Adv. Nat. Sci. Nanosci. Nanotechnol.* **3**, 035005 (2012)
38. S. Muthukumar, R. Gopalakrishnan, *Opt. Mater.* **34**, 1946–1953 (2012)
39. K. Kumar, M. Chitkara, I.S. Sandhu, D. Mehta, S. Kumar, *J. Alloy. Compd.* **588**, 681–689 (2014)
40. K. Raja, P.S. Ramesh, D. Geetha, *Spectrochim. Acta A* **131**, 183–188 (2014)
41. P. Dhamodharan, R. Gobi, N. Shanmugam, N. Kannadasan, R. Poonguzhali, S. Ramya, *Spectrochim. Acta A* **131**, 125–131 (2014)
42. G. Xiong, L. Luo, C. Li, X. Yang, *Energ. Fuels* **23**, 1342–1346 (2009)
43. M.Z. Hussein, S.H. Al Ali, Z. Zainal, M.N. Hakim, *Int. J. Nanomed.* **6**, 1373–1383 (2011)
44. A.N. Gruzintsev, V.T. Volkov, C. Barthou, P. Benalloul, J. Frigerio, *Thin Solid Films* **459**, 262–266 (2004)
45. Y. Zhang, B. Lin, Z. Fu, C. Liu, W. Han, *Opt. Mater.* **28**, 1192–1196 (2006)
46. V. Gandhi, R. Ganesan, H. Hameed, A. Syedahamed, M. Thayanan, *J. Phys. Chem. C* **118**, 9715–9725 (2014)
47. P. Li, S. Wang, J. Li, Y. Wei, *J. Lumin.* **132**, 220–225 (2012)
48. D.H. Xu, W.Z. Shen, *J. Phys. Chem. C* **116**, 13368–13373 (2012)
49. R. Udayabhaskar, R.V. Mangalaraja, B. Karthikeyan, *J. Mater. Sci. Mater. Electron.* **24**, 3183–3188 (2013)
50. D. Liu, Y. Lv, M. Zhang, Y. Liu, Y. Zhu, R. Zong, Y. Zhu, *J. Mater. Chem. A* **2**, 15377 (2014)
51. Y. Hong, C. Tian, B. Jiang, A. Wu, Q. Zhang, G. Tian, H. Fu, *J. Mater. Chem. A* **1**, 5700–5708 (2013)
52. S.Y. Kim, T.H. Lim, T.S. Chang, C.H. Shin, *Catal. Lett.* **117**, 112–118 (2007)
53. P. Jongnavakit, P. Amornpitoksuk, S. Suwanboon, N. Ndiege, *Appl. Surf. Sci.* **258**, 8192–8198 (2012)
54. W.-W. Wang, Y.-J. Zhu, L.-X. Yang, *Adv. Funct. Mater.* **17**, 59–64 (2007)
55. M. Ferhat, A. Zaoui, R. Ahuja, *Appl. Phys. Lett.* **94**, 142502 (2009)
56. C.-J. Chang, T.-L. Yang, Y.-C. Weng, *J. Solid State Chem.* **214**, 101–107 (2014)
57. D. Chen, Z. Wang, T. Ren, H. Ding, W. Yao, R. Zong, Y. Zhu, *J. Phys. Chem. C* **118**, 15300 (2014)
58. R.C. Pawar, D.H. Choi, J.S. Lee, C.S. Lee, *Mater. Chem. Phys.* **151**, 167–180 (2015)